

**INSERT CREATIVE NAME HERE**

Author's name

Bachelorarbeit in Physik  
angefertigt im Argelander-Institut für Astronomie

vorgelegt der  
Mathematisch-Naturwissenschaftlichen Fakultät  
der  
Rheinischen Friedrich-Wilhelms-Universität  
Bonn

MMM 2024

DRAFT

Ich versichere, dass ich diese Arbeit selbstständig verfasst und keine anderen als die angegebenen Quellen und Hilfsmittel benutzt sowie die Zitate kenntlich gemacht habe.

Bonn, .....

Datum

.....

Unterschrift

1. Gutachter: Prof. Dr. John Smith
2. Gutachterin: Prof. Dr. Anne Jones

---

## Acknowledgements

---

I would like to thank ...

You should probably use \chapter\* for acknowledgements at the beginning of a thesis and \chapter for the end.

DRAFT

---

# Contents

---

<b>1</b>	<b>Introduction</b>	<b>1</b>
<b>2</b>	<b>Theoretical Background</b>	<b>2</b>
2.1	Clusters and groups of galaxies . . . . .	2
2.1.1	The Intracluster Medium (ICM) . . . . .	2
2.1.2	Emission Processes within the ICM . . . . .	2
2.1.3	The galaxy group NGC1550 . . . . .	3
2.2	eROSITA . . . . .	3
2.3	Skybackground and contamination sources . . . . .	3
<b>3</b>	<b>Data Reduction</b>	<b>5</b>
3.1	Raw photon images . . . . .	5
3.2	Image filtering . . . . .	5
3.3	PIB Correction . . . . .	6
3.4	Absorption Correction . . . . .	7
3.5	Exposure Correction . . . . .	7
3.6	Wavelet filtering and Point Source Removal . . . . .	8
<b>4</b>	<b>Data Analysis</b>	<b>10</b>
4.1	Image Inspection . . . . .	10
4.2	Surface Brightness Analysis . . . . .	10
4.2.1	Full Azimuthal Surface Brightness . . . . .	10
4.2.2	Beta Model and Residual Image . . . . .	13
<b>A</b>	<b>Appendix</b>	<b>16</b>
A.1	PIB Map . . . . .	16
	<b>Bibliography</b>	<b>17</b>
	<b>List of Figures</b>	<b>19</b>
	<b>List of Tables</b>	<b>20</b>

# CHAPTER 1

---

## Introduction

---

Testing Kolokythas et al., 2020. new line

# CHAPTER 2

---

## Theoretical Background

---

### 2.1 Clusters and groups of galaxies

Throughout the Universe, galaxies are not distributed homogeneously but are instead aggregated into massive cosmic structures known as galaxy groups or galaxy clusters. Galaxy clusters – the largest relaxed structures in the Universe – typically have masses exceeding  $M \gtrsim 3 \times 10^{14} M_{\odot}$ , whereas galaxy groups have masses around  $M \sim 3 \times 10^{13} M_{\odot}$  (Schneider, 2006). Advancements in X-ray astronomy have demonstrated that these structures are significant sources of X-ray radiation (Cavaliere, Gurkaynak, and Tucker, 1971). This emission is well understood to originate from a hot intergalactic gas known as the intracluster medium (ICM), which is characterized by temperatures in the range of  $10^7$  to  $10^8$  K and constitutes the primary baryonic component of galaxy clusters (Schneider, 2006).

#### 2.1.1 The Intracluster Medium (ICM)

Within the deep gravitational wells of galaxy clusters, the temperatures become sufficiently high to fully ionize lighter elements and partially ionize heavier elements, resulting in the formation of a plasma. This hot, diffuse, and optically thin plasma, known as the Intracluster Medium (ICM), emits significant amounts of X-ray radiation. X-ray analysis of the ICM have enabled a wide variety of cosmological studies, including large-scale structure formation in the Universe (Kravtsov and Borgani, 2012).

#### 2.1.2 Emission Processes within the ICM

A key principle of electrodynamics is that accelerated charges radiate energy. This radiation is referred to as bremsstrahlung or "free-free" when a free charged particle, typically an electron, is accelerated by the electric field of other charges, usually ions. In the ICM, this process predominates at temperatures above  $k_B T_e \gtrsim 2 \text{ keV}$ , where the total emissivity at solar metallicity scales approximately as

$$\epsilon_{\text{ff}} \propto T_e^{\frac{1}{2}} n_e,$$

with  $n_e$  and  $T_e$  as the electron number density and temperature, respectively. At lower temperatures ( $k_B T \lesssim 2 \text{ keV}$ ), line emission becomes significant, with the emissivity being roughly described by

$$\epsilon \propto T_e^{-0.6} n_e.$$

### 2.1.3 The galaxy group NGC1550

Insert cool stuff about cluster here

## 2.2 eROSITA

The extended ROentgen Survey with an Imaging Telescope Array (eROSITA) is a highly sensitive, wide-field X-ray telescope designed to capture deep and precise images across large areas of the sky. Mounted on the Spektrum-Roentgen-Gamma (SRG) observatory in a halo orbit around the second Lagrange Point, eROSITA operates within the 0.2 to 10.0 keV energy range. It is the first instrument to perform an all-sky imaging survey in the hard X-ray band (2.0 to 10.0 keV). In the soft X-ray band (0.5 to 2.0 keV), eROSITA boasts a sensitivity that is approximately 20 times greater than that of its predecessor, the ROSAT All-Sky Survey. eROSITA features seven identical mirror modules, known as Telescope Modules (TMs), each with 54 mirror shells in Wolter-I geometry and a 1.6-meter focal length. Five TMs (TM1, TM2, TM3, TM4, TM6) have aluminum on-chip optical light filters and are collectively referred to as TM8. The remaining two TMs (TM5, TM7), designed for low-energy spectroscopy, lack these filters and are referred to as TM9. (Predehl et al., 2021). Collectively, TM8 and TM9 are referred to as TM0.

## 2.3 Skybackground and contamination sources

For a thorough analysis of X-ray photons, it is essential to carefully consider both external background and internal instrumental contamination effects. The following section will provide a brief overview of the most important factors relevant to this analysis.

**Cosmic X-ray Background (CXB):** The Cosmic X-ray background comprises multiple sources, including diffuse, unabsorbed thermal emissions from the Local Hot Bubble, a plasma cavity surrounding the Sun, and absorbed thermal emissions from the Galactic halo (Galeazzi et al., 2006). Additionally, it includes discrete extragalactic sources, predominantly unresolved AGNs (Brandt and Hasinger, 2005). The diffuse component is more prominent in the lower energy band  $\sim 1 \text{ keV}$ , while the extragalactic sources dominate at higher energies.

**Non-X-ray Background (NXB):** The non-X-ray background consists of two main components: highly variable soft protons flares from the solar corona and Earth's magnetosphere, which can be focused onto detectors, and energetic Galactic Cosmic Ray (GCR) primaries, which interact with the detector to produce secondary particles. While primary GCR events can be mostly discarded by

onboard processing, the secondary particles deposit charge in the detector, making it challenging to distinguish them from true X-ray events. (Bulbul et al., 2020)

**eROSITA light leak:** Shortly after the launch of eROSITA, it was observed that CCDs lacking an on-chip filter (TM9) recorded a notably higher number of events. This was attributed to optical and ultraviolet light from the Sun entering the CCD through an unidentified gap in the detector shielding and was subsequently termed “light-leak” (Predehl et al., 2021).

**$N_{\text{H}}$  absorption:** As X-rays travel to the detector, they undergo photoelectric absorption in the interstellar and intergalactic medium. The cross-section  $\sigma \propto E^{-3.5}$  is inversely proportional to energy, causing a bias toward harder X-rays, as they interact less. Additionally,  $\sigma \propto Z^5$  making metal abundance crucial for energies  $\gtrsim 0.2 \text{ keV}$ .

Table 2.1: Fit Parameters

Region	1	2	3	4
West	$(2.38 \times 10^{-5})$	$(5.47 \times 10^{-1})$	$(1.11 \times 10^2)$	$(1.01 \times 10^{-7})$
East	$(2.31 \times 10^{-5})$	$(4.96 \times 10^{-1})$	$(9.2 \times 10^1)$	$(1.05 \times 10^{-7})$
North	$(1.69 \times 10^{-5})$	$(4.53 \times 10^{-1})$	$(8.1 \times 10^1)$	$(8.08 \times 10^{-8})$
South	$(4.72 \times 10^{-5})$	$(4.99 \times 10^{-1})$	$(6.67 \times 10^1)$	$(9.53 \times 10^{-8})$

# CHAPTER 3

---

## Data Reduction

---

In the following section, the underlying data shall be reduced and corrected for the various effects and contamination sources explained in Section 2.3. Data from eRASSX is utilized for all TMs (1-7) using *eROSITA* pipeline processing version c010. The galaxy group NGC1550 is located in skytile 065087. In addition, the surrounding skytiles 062084, 062087, 062090, 065084, 065090, 068084, 068087, 068090 are used to encompass regions up to  $\sim 3R_{200}$ . The data reduction is performed with the software HEASoft version XXX and the extended Science Analysis Software System (eSASS 4DR1). Images were created using astropy.

### 3.1 Raw photon images

Before the data reduction process, raw photon images for all combined skytiles and TMs are presented across the following energy bands: 0.2 to 2.3 keV, 2.3 to 6.0 keV, and 6.0 to 9.0 keV. The skytiles were combined using the *eSASS* task `evtool`, with no additional parameters applied to reveal all inherent deficiencies in the raw images. The raw photon images are presented in 3.1. As observed, most cluster emission is concentrated in the lower energy band, making it the focus for detecting emission structures. In this analysis, the 0.2 to 2.3 keV energy band is used. Due to the light-leak in TM9, however, the energy range is restricted to 0.8 to 2.3 keV, while for TM8 it remains 0.2 to 2.3 keV. Hereafter, this TM-dependent energy band will be referred to as the “soft band” and the 6.0 to 9.0 keV energy range as the “hard band”.

### 3.2 Image filtering

Each skytile is cleaned individually using `evtool` with `pattern=15` to select all event patterns and `flag=0xc00fff30` to remove bad pixels and CCD corners. Subsequently, soft proton flares are identified and mitigated through the following process: the `flaregti` task is used to generate light curves with 20 s time bins in the energy range of 5 to 10 keV. A  $3\sigma$  threshold is determined; time intervals exceeding this threshold indicate elevated count rates likely due to soft proton flares. The task `flaregti` is then rerun using this threshold to establish good-time-intervals (GTIs) excluding these

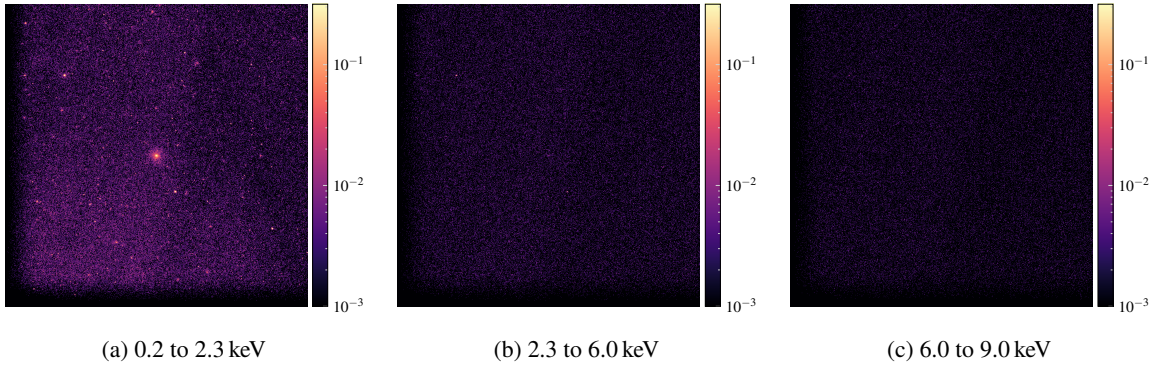


Figure 3.1: Raw photon images from TM0 of all combined skytiles centered around NGC1550, displayed in the energy bands 0.2 to 2.3 keV, 2.3 to 6.0 keV, and 6.0 to 9.0 keV, with Gaussian smoothing of 4 pixels applied. The colorbar represents (smoothed) photon counts. Most of the cluster emission is visible in the lower energy band (0.2 to 2.3 keV). A noticeable count drop on the right side of the images is evident and will be addressed through the exposure map correction detailed in Section X.

flare periods, which are applied using `evtool` with the `gti="FLAREGTI"` parameter. All SPF-filtered and cleaned skytiles are combined into a single TM0 photon image using `evtool`. Hereafter, these combined images shall be referred to as “filtered”. The `evtool` task with the `telid` parameter is also used to split the filtered photon images into individual filtered images for each TM, as needed for subsequent steps.

### 3.3 PIB Correction

Subtracting the particle-induced background (PIB) from the combined filtered photon image is necessary. The following approach is based on extensive studies of the *eROSITA* FWC data conducted by Dr. F. Pacaud, as utilized for example in Reiprich et al., 2021. The PIB is modeled for each TM using filter wheel closed (FWC) data. Due to the minimal spatial variation of the PIB, this modeling utilizes the flat exposure map created with the *eSASS* task `expmap`. Furthermore, given the negligible spectral variation, the counts  $H_{\text{obs}}$  in the hard band, where PIB counts dominate, is used to estimate the PIB contribution in the soft bands by multiplication with the ratio  $R$  of the number of FWC counts in the soft band  $S_{\text{FWC}}$  to the hard band  $H_{\text{FWC}}$ . A background map for each TM is then generated by applying this factor to the flat exposure map, normalized to 1 by dividing by the sum of all pixel values (norm. exposure map). Hence, the PIB map of a given TM is given by

$$\text{PIB map}_{\text{TM}} = H_{\text{obs}} R \cdot (\text{norm. exposure map})$$

PIB corrected image are obtained by subtracting the PIB map of each TM from the respective filtered photon image. The complete image for TM0 is obtain by co-adding all PIB corrected images. Furthermore, individual background maps are also co-added to form a complete PIB map, which can be found in Appendix A.1. Figure ?? compares the TM0 filtered image before and after PIB correction.

### 3.4 Absorption Correction

As discussed in Section 2.3, X-ray absorption by the ISM must be considered. The methodology outlined in Willingale et al., 2013 is followed. Additionally, scripts for the absorption correction were provided by Angie Veronica (Veronica, 2020). At higher energies ( $\gtrsim 0.2$  keV), as is relevant for this analysis, absorption from metals play a significant role. Assuming solar metallicity, the hydrogen column density  $N_{\text{H}}$  can be used to trace the absorbing material. A cutout of the HI4PI all-sky survey (HI4PI Collaboration et al., 2016) is reprojected onto relevant sky tiles to create a neutral atomic hydrogen map ( $N_{\text{HI}}$ -map). Additionally, a molecular hydrogen map ( $N_{\text{H}_2}$ -map) is constructed by dividing the full sky image into  $52 \times 52$  pixel cells, querying  $N_{\text{H}_2}$  values from the Swift homepage<sup>1</sup>, and distributing these values across each cell. The total  $N_{\text{Htot}}$ -map, constructed by  $N_{\text{Htot}} = N_{\text{H}} + 2N_{\text{H}_2}$ , is shown in Appendix B, with  $N_{\text{H}}$  ranging from  $N_{\text{Htot}, \text{min}} = 2.91 \times 10^{20} \text{ cm}^{-2}$  to  $N_{\text{Htot}, \text{max}} = 1.61 \times 10^{21} \text{ cm}^{-2}$ . Next, for each individual  $N_{\text{H}}$ -value in the  $N_{\text{Htot}}$ -map, the expected soft band count rates for TM1 and TM5 are simulated for the model

$$\text{apc}_{\text{LHB}} + \text{ph}_{\text{abs.}} \cdot (\text{apc}_{\text{MWH}} + \text{pow}).$$

using XSPEC<sup>2</sup> with the `fakeit` command and their respective area (ARF) and response files (RMF). Here,  $\text{apc}_{\text{LHB}}$  represents unabsorbed Local Hot Bubble emission,  $\text{ph}_{\text{abs.}}$  the absorption along the line of sight,  $\text{apc}_{\text{MWH}}$  the absorbed Milky Way Halo emission, and  $\text{pow}$  the absorbed emission from unresolved point sources (e.g., AGNs). A correction factor  $A_{\text{corr}}$  is determined for each value of  $N_{\text{H}}$  by dividing the simulated count rate for the  $N_{\text{H}}$ -map median ( $\overline{N_{\text{Htot}}}$ ) by the simulated count rate of the  $N_{\text{H}}$  of interest, hence

$$A_{\text{corr}}(N_{\text{H}}) = \frac{\text{simulated count rate}(\overline{N_{\text{Htot}}})}{\text{simulated count rate}(N_{\text{H}})}.$$

Finally, each  $N_{\text{H}}$  in the  $N_{\text{Htot}}$ -map is replaced by the corresponding correction factor  $A_{\text{corr}}$  to create an absorption correction map. Absorption correction maps are created for both TM1 and TM5, which serve as proxies for TM8 and TM9, respectively, due to their similar response files, and will be utilized in the subsequent steps.

### 3.5 Exposure Correction

The counts image of any given X-ray observation inherently depends on a detector's effective area and the telescope's pointing motion throughout the observation. To obtain meaningful flux units (e.g.  $\text{cts} \cdot \text{arcsecond}^{-2} \text{s}^{-1}$ ), these effects must be considered. This is achieved by dividing the count image by an exposure map, thereby rescaling all segments of the count image to the same relative exposure (Davis, 2001). However, an exposure map must be created separately for TM8 and TM9 due to three reasons: first, TM9 uses a narrow energy band, which lowers its expected count rate;

<sup>1</sup> <https://www.swift.ac.uk/analysis/nhtot/index.php> (Last accessed: 25.07.2024)

<sup>2</sup> <https://heasarc.gsfc.nasa.gov/xanadu/xspec/> (Last accessed: 25.07.2024)

second, this narrower energy band necessitates a different absorption correction map; third, TM8 and TM9 have very distinct response files because of their different filter configurations. Thus, both exposure maps cannot simply be combined but must be corrected for these effects. The procedure outlined in Reiprich et al., 2021 will be followed. First, the exposure map of TM8 and TM9 are divided by their respective absorption correction maps to obtain an absorption-corrected exposure map ( $\text{exmap}_{\text{TM8, corr}}$ ,  $\text{exmap}_{\text{TM9, corr}}$ ). Second, the ratio of PIB-corrected count rates of TM8 and TM9 is used to define a correction factor

$$E_{\text{corr}} = \frac{\text{PIB corr. count rate(TM9)}}{\text{PIB corr. count rate(TM9)}}$$

The total absorption-corrected exposure map for TM0 is then given by

$$\text{exmap}_{\text{TM0, corr}} = \text{exmap}_{\text{TM8, corr}} + E_{\text{corr}} \cdot \text{exmap}_{\text{TM9, corr}}$$

Dividing the PIB-corrected TM0 image by the complete absorption-corrected exposure map leads to the final filtered, PIB-corrected, absorption-corrected, exposure-corrected image.

### 3.6 Wavelet filtering and Point Source Removal

It is necessary to remove the emission from point-like sources (e.g. AGNs) to prevent interference with the cluster emission under study. This is achieved using the wavelet filtering pipeline as described in Pacaud et al., 2006. Wavelet transformation decomposes an image  $I(x, y)$  into coefficients  $(w_1, \dots, w_n, c_n)$

$$I(x, y) = c_n(x, y) + \sum_{j=1}^n w_j(x, y).$$

Here,  $c_n(x, y)$  is the smoothed image, and  $w_j(x, y)$  represents the contribution of a wavelet function at a scale  $j$  and position  $(x, y)$  to the total image. By retaining only the coefficients that satisfy

$$|w_j(x, y)| > k\sigma_j,$$

where  $\sigma_j$  is the standard deviation at scale  $j$  and  $k$  is a clipping factor, and then applying the inverse wavelet transformation, an image is obtained that includes only significant scales, i.e. those not due to noise (Starck, J.-L. and Pierre, M., 1998). The resultant image is referred to as a wavelet-filtered image. In the pipeline being used, the absorption-corrected exposure map,  $\text{exmap}_{\text{TM0, corr}}$ , and the raw photon image are used to account for previous data reduction and to statistically handle the Poisson noise. After wavelet filtering, a source catalogue is obtained running SExtractor (Bertin and Arnouts, 1996). This is enabled by the significant noise reduction and smoothed background achieved by wavelet filtering. The extended emission near NGC1550 is manually removed, and a cheese mask is created from the catalog and applied to  $\text{exmap}_{\text{TM0, corr}}$ . Unrelated emission around IC366 is also manually added to the mask. Rerunning wavelet filtering with the cheese-masked map reduces ringing artifacts, which typically occur near steep flux gradients. Figure 3.2 compares the

wavelet filtering before and after application of the cheese-mask to the exposure map.

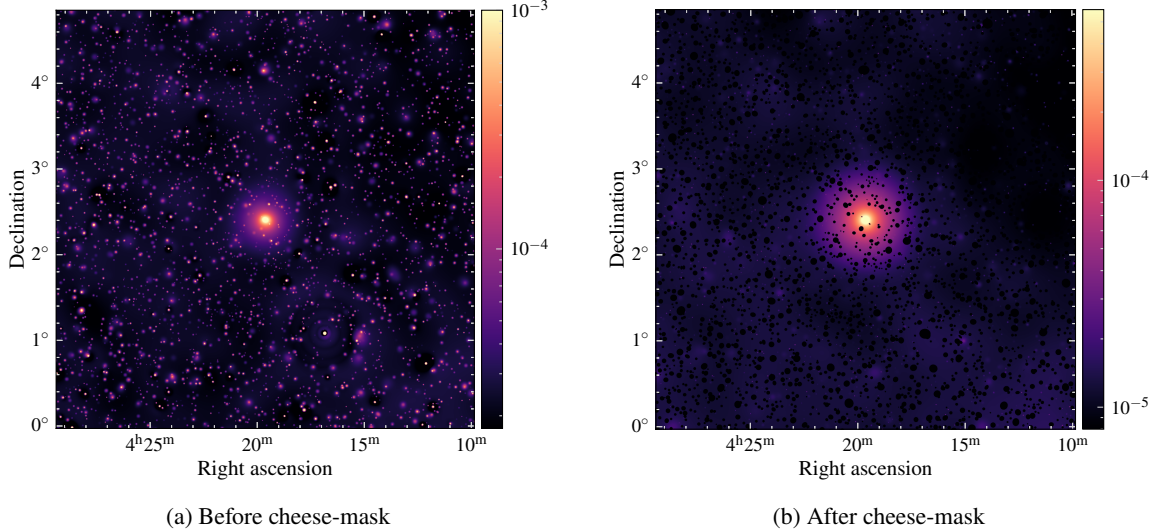


Figure 3.2: Corrected wavelet filtered image before (left) and after (right) applying the cheesemask created with SExtractor. The left image is normalized such that the ringing artifacts are most prominent, for example around IC366 ( $\sim (4^{\text{h}} 16^{\text{m}}, 1.05^{\circ})$ ). The cheese-masked imaged has significantly reduced ringing artifacts.

# CHAPTER 4

---

## Data Analysis

---

### 4.1 Image Inspection

For a clearer visualization of the emission structures, a contour plot of the corrected wavelet-filtered image is presented (Figure 4.1). The group exhibits a spherically symmetrical appearance, with a distinct emission boundary clearly visible at  $R_{500}$ . Furthermore, emission beyond  $R_{500}$  and  $R_{200}$  is difficult to distinguish from the complex background. A noticeable asymmetry is observed in the background emission, with a drop-off to the north compared to the south.

### 4.2 Surface Brightness Analysis

#### 4.2.1 Full Azimuthal Surface Brightness

To more accurately identify or exclude potential deviations from spherical symmetry, surface brightness analysis will be performed. First, the emission center is estimated by constructing a  $2'$  aperture around the apparent center, as given in Section X. This aperture size is chosen to capture a statistically significant number of photons without leaving the group center. The flux-weighted average of the image coordinates within this aperture yields a right ascension of  $64.909^\circ$  and a declination of  $2.414^\circ$ . Concentric Anulli of  $1'$  width are constructed from the calculated flux-weighted surface brightness of the group up to an angular distance of  $80' \sim 1.5R_{200}$ . The counts  $C$  within each annulus are determined using the `funcnts` task from the `fntools` software, with a Poisson error of  $\sqrt{C}$ . The surface brightness  $S$  for each annulus is calculated by

$$S = \frac{C_{\text{image}} - C_{\text{PIB}}}{C_{\text{expmap}} \cdot A},$$

where  $C$  denotes the counts in the photon image, total PIB map, and exposure map, respectively. Errors are calculated using Gaussian error propagation. Furthermore, background estimation is performed using 10 circular regions with a  $48'$  radius, each centered  $160'$  from the calculated center of NGC 1550. The average background surface brightness is evaluated for all circles combined and

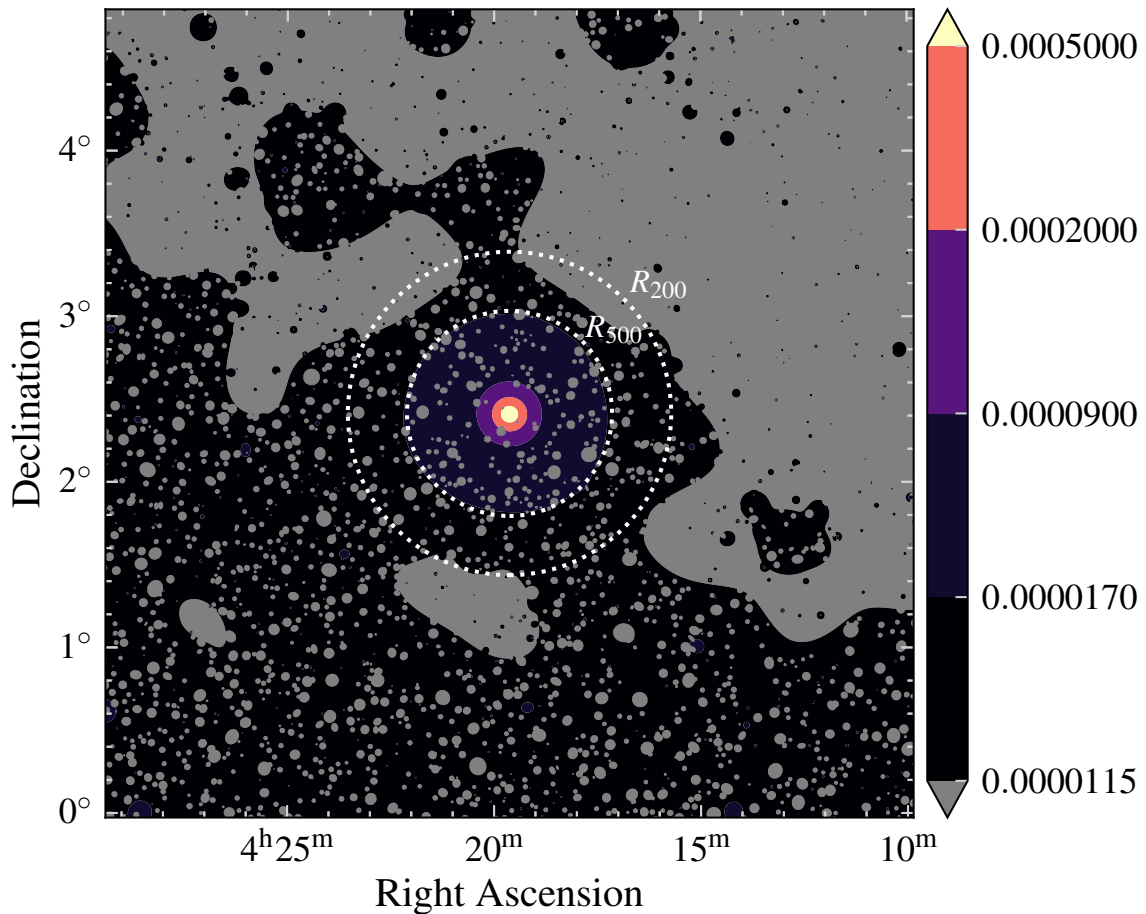


Figure 4.1: Contour plot of the corrected wavelet-filtered image. The colorbar represents counts per second. A distinct emission cut is visible at  $R_{500}$ , while the emission beyond  $R_{500}$  is difficult to discern from the background.

separately for the northern (Circles 1-5) and southern region (Circles 6-10) to account for the possibly significant background gradient. Table 4.1 lists the average background for all 3 cases. As is clear from the table, all background values consist with each other within a  $1\sigma$ -Intervall. Thus, for the following analysis and interpretation, the total background value obtained from all circles is utilized.

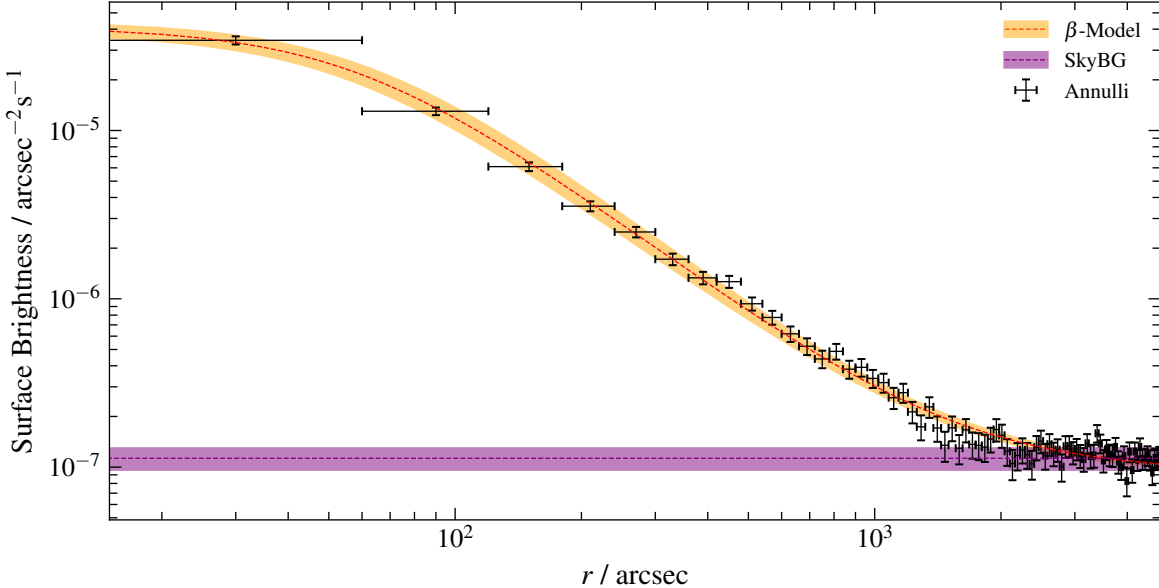


Figure 4.2: Surface Brightness within each annulus (black crosses) as a function of distance from the determined SB-center. The dashed orange line represents the best  $\beta$ -model fit, while the purple line indicates the observationally determined background. The shaded regions correspond to their respective  $1\sigma$  intervals.

Region	Background ( $\text{cts s}^{-1} \text{arcsec}^{-2}$ )
Southern Background	$13 \times 10^{-8} \pm 2.0 \times 10^{-9}$
Northern Background	$9.9 \times 10^{-8} \pm 1.2 \times 10^{-8}$
Total Background	$11 \times 10^{-8} \pm 1.7 \times 10^{-8}$

Table 4.1: Average background surface brightness for southern, northern, and total regions in units of counts per second per square arcsecond ( $\text{cts s}^{-1} \text{arcsec}^{-2}$ ).

A  $\beta$ -Model is employed to characterize the surface brightness profile, given by

$$S(r) = S_0 \left( 1 + \left( \frac{r}{r_c} \right)^2 \right)^{-3\beta+0.5} + d$$

where  $d$  represents the background level. The center of each annulus is taken to be  $r$  and the corresponding surface brightness values are utilized. The optimized parameters and  $\chi^2/\text{d.o.f}$  (Chi

squared per degrees of freedom) are listed in Table 4.2. Figure 4.2 illustrates the surface brightness as a function of radial distance from the center, including both the fitted  $\beta$ -Model and the observationally estimated background level. As one can clearly see from 4.2 and the  $\chi^2/\text{d.o.f}$  value of 0.96, the beta

Parameter	$S_0$	$\beta$	$r_c$	$d$
	$(4.1 \pm 0.4) \times 10^{-5}$	$0.478 \pm 0.008$	$60 \pm 5$	$(9.3 \pm 0.4) \times 10^{-8}$
$\chi^2/\text{d. o. f}$	0.96			

Table 4.2: Fit parameters, their errors, and the reduced chi-squared value.

model describes the surface brightness profile well and a value of  $\beta = 0.478 \pm 0.008$  is obtained. This is consist with the findings of THE ALMIGHTY FLYING SPAGHETTI MONSTER. The estimated and fitted backgrounds are consistent. A two-beta model fit, however, was not successful. This can be attributed to the limited angular resolution in the core region and the degeneracy between the core radius and  $\beta$ .

#### 4.2.2 Beta Model and Residual Image

Using the parameters from Table 4.1, a beta model image (Fig. 4.3(a)) and a residual image (Fig. 4.3(b)) are created. The beta model image is generated by distributing the one-dimensional beta model across the image. This involves computing the distance from the surface brightness center to each coordinate  $(x, y)$  in the image and then scaling the output of the beta model by the eROSITA pixel area of  $16\text{arcsec}^2$ . The residual image was obtained by subtracting the scaled beta model from the fully corrected image:

$$\text{res. img}(x, y) = \text{corr. img}(x, y) - S(\sqrt{x^2 + y^2}) \cdot \text{pix. area}$$

The residual image reveals that, except at the very center of the galaxy group, the beta model slightly overestimates the emission around the core. This overestimation can be attributed to the absence of a second beta component, as a single beta model often inadequately describes the inner core emission, leading to higher-than-expected values.

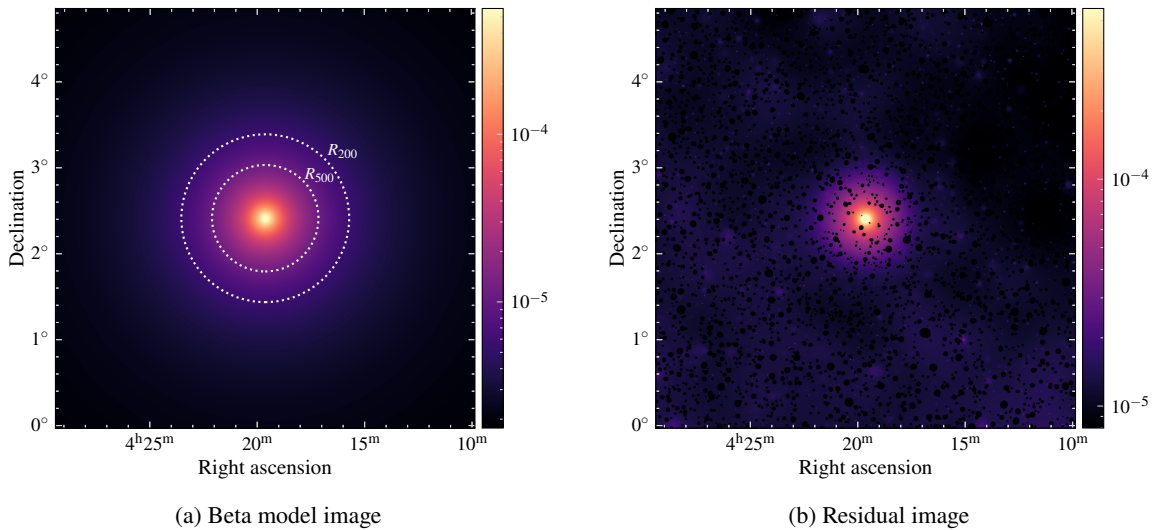


Figure 4.3: Comparison of the beta model image and the residual image. The colorbar indicates counts per second. The residual image indicate that the beta model slightly overestimates the emission around the core, likely due to the inadequacy of a single beta model in capturing the core's emission.

# **Appendix**

# APPENDIX A

---

## Appendix

---

### A.1 PIB Map

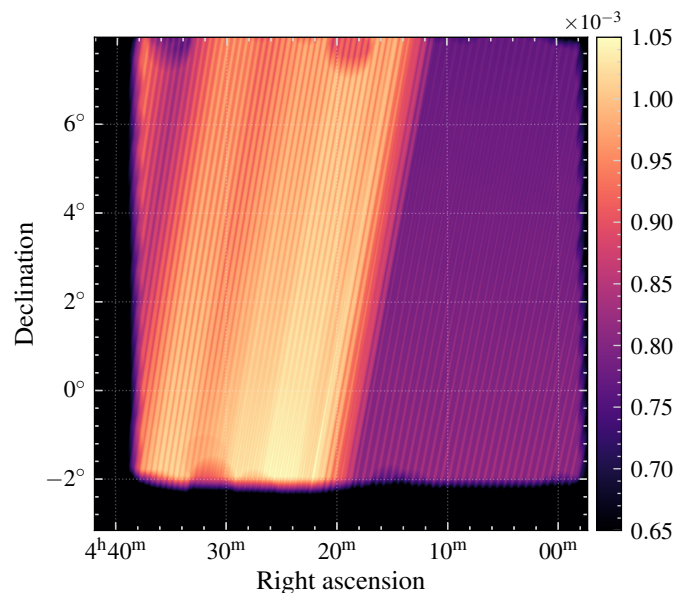


Figure A.1: PIB map created by co-adding individual background maps for each telescope module (TM).

---

## Bibliography

---

- Bertin, E. and S. Arnouts (1996), *SExtractor: Software for source extraction.*, **117** 393 (cit. on p. 8).
- Brandt, W. and G. Hasinger (2005), *Deep Extragalactic X-ray Surveys*, Annual Review of Astronomy and Astrophysics **43** 827, First published online as a Review in Advance on June 14, 2005 (cit. on p. 3).
- Bulbul, E. et al. (2020), *Characterization of the Particle-induced Background of XMM-Newton EPIC-pn: Short- and Long-term Variability*, The Astrophysical Journal **891** 13, URL: <https://dx.doi.org/10.3847/1538-4357/ab698a> (cit. on p. 4).
- Cavaliere, A. G., H. Gurksy, and W. H. Tucker (1971), *Extragalactic X-ray Sources and Associations of Galaxies*, Nature **231** 437, ISSN: 1476-4687, URL: <https://doi.org/10.1038/231437a0> (cit. on p. 2).
- Davis, J. E. (2001), *The Formal Underpinnings of the Response Functions Used in X-Ray Spectral Analysis*, The Astrophysical Journal **548** 1010, © 2001. All rights reserved. Printed in U.S.A. (cit. on p. 7).
- Galeazzi, M., A. Gupta, K. Covey, and E. Ursino (2006), *XMM-Newton observations of the diffuse X-ray background*, Department of Physics, University of Miami (cit. on p. 3).
- HI4PI Collaboration et al. (2016), *HI4PI: A full-sky HI survey based on EBHIS and GASS*, Astronomy & Astrophysics **594** A116, URL: <https://ui.adsabs.harvard.edu/abs/2016A&A...594A.116H> (cit. on p. 7).
- Kolokythas, K. et al. (2020), *Evidence of AGN feedback and sloshing in the X-ray luminous NGC 1550 galaxy group*, Monthly Notices of the Royal Astronomical Society **496** 1471, ISSN: 1365-2966, URL: <http://dx.doi.org/10.1093/mnras/staa1506> (cit. on p. 1).
- Kravtsov, A. V. and S. Borgani (2012), *Formation of Galaxy Clusters*, Annual Review of Astronomy and Astrophysics **50** 353, ISSN: 0066-4146, eprint: <https://www.annualreviews.org/doi/pdf/10.1146/annurev-astro-081811-125502>, URL: <https://www.annualreviews.org/doi/10.1146/annurev-astro-081811-125502> (cit. on p. 2).
- Pacaud, F. et al. (2006), *The XMM Large-Scale Structure survey: the X-ray pipeline and survey selection function*, Monthly Notices of the Royal Astronomical Society **372** 578, ISSN: 0035-8711, eprint: <https://academic.oup.com/mnras/article-pdf/372/2/578/2937517/mnras0372-0578.pdf>, URL: <https://doi.org/10.1111/j.1365-2966.2006.10881.x> (cit. on p. 8).
- Predehl, P. et al. (2021), *First science highlights from SRG/eROSITA: The eROSITA X-ray telescope on SRG*, A&A **647** A1 (cit. on pp. 3, 4).

## Bibliography

---

- Reiprich, T. H. et al. (2021), *The Abell 3391/95 galaxy cluster system: A 15 Mpc intergalactic medium emission filament, a warm gas bridge, infalling matter clumps, and (re-) accelerated plasma discovered by combining SRG/eROSITA data with ASKAP/EMU and DECam data*, *AandA* **647** A2, URL: <https://doi.org/10.1051/0004-6361/202039590> (cit. on pp. 6, 8).
- Schneider, P. (2006), *Extragalactic Astronomy and Cosmology: An Introduction*, Second Edition, Springer-Verlag Berlin Heidelberg 2006, ISBN: 978-3-642-54082-0 (cit. on p. 2).
- Starck, J.-L. and Pierre, M. (1998), *Structure detection in low intensity X-ray images*, *Astron. Astrophys. Suppl. Ser.* **128** 397, URL: <https://doi.org/10.1051/aas:1998150> (cit. on p. 8).
- Veronica, A. (2020), *X-ray Studies of the Interacting Galaxy Cluster System Abell 3391 and Abell 3395 Using eROSITA and XMM-Newton*, Masterthesis in Astrophysics, MA thesis: Argelander-Institut für Astronomie, Mathematisch-Naturwissenschaftliche Fakultät der Rheinischen Friedrich-Wilhelms-Universität Bonn (cit. on p. 7).
- Willingale, R., R. L. C. Starling, A. P. Beardmore, N. R. Tanvir, and P. T. O'Brien (2013), *Calibration of X-ray absorption in our Galaxy*, *431* 394, arXiv: [1303.0843 \[astro-ph.HE\]](https://arxiv.org/abs/1303.0843) (cit. on p. 7).

---

## List of Figures

---

3.1	Raw photon images from TM0 of all combined skytiles centered around NGC1550, displayed in the energy bands 0.2 to 2.3 keV, 2.3 to 6.0 keV, and 6.0 to 9.0 keV, with Gaussian smoothing of 4 pixels applied. The colorbar represents (smoothed) photon counts. Most of the cluster emission is visible in the lower energy band (0.2 to 2.3 keV). A noticeable count drop on the right side of the images is evident and will be addressed through the exposure map correction detailed in Section X. . . . .	6
3.2	Corrected wavelet filtered image before (left) and after (right) applying the cheesemask created with SExtractor. The left image is normalized such that the ringing artifacts are most prominent, for example around IC366 ( $\sim (4^h 16^m, 1.05^\circ)$ ). The cheese-masked imaged has significantly reduced ringing artifacts. . . . .	9
4.1	Contour plot of the corrected wavelet-filtered image. The colorbar represents counts per second. A distinct emission cut is visible at $R_{500}$ , while the emission beyond $R_{500}$ is difficult to discern from the background. . . . .	11
4.2	Surface Brightness within each annulus (black crosses) as a function of distance from the determined SB-center. The dashed orange line represents the best $\beta$ -model fit, while the purple line indicates the observationally determined background. The shaded regions correspond to their respective $1\sigma$ intervals. . . . .	12
4.3	Comparison of the beta model image and the residual image. The colorbar indicates counts per second. The residual image indicate that the beta model slightly overestimates the emission around the core, likely due to the inadequacy of a single beta model in capturing the core's emission. . . . .	14
A.1	PIB map created by co-adding individual background maps for each telescope module (TM). . . . .	16

---

## List of Tables

---

2.1	Fit Parameters . . . . .	4
4.1	Average background surface brightness for southern, northern, and total regions in units of counts per second per square arcsecond ( $\text{cts s}^{-1} \text{arcsec}^{-2}$ ) . . . . .	12
4.2	Fit parameters, their errors, and the reduced chi-squared value. . . . .	13